Sheffield Hallam University

Photo-Fenton degradation of methylene blue using hematite-enriched slag under visible light

ALI, Ahmed, KHAN, Irfan, ZHANG, Bofan, NOMURA, Kiyoshi, HOMONNAY, Zoltan, KUZMANN, Erno, SCRIMSHIRE, Alex, BINGHAM, Paul <http://orcid.org/0000-0001-6017-0798>, KREHULA, Stjepko, MUSIC, Svetozar, AKIYAMA, Kazuhiko and KUBUKI, Shiro

Available from Sheffield Hallam University Research Archive (SHURA) at:

http://shura.shu.ac.uk/26378/

Published version

Copyright and re-use policy

1 # Title page

2 **Names of the authors:**

3 Ahmed S. Ali[1], Irfan Khan[1], Bofan Zhang[1], Kiyoshi Nomura[1], Zoltan Homonnay[2], Erno
4 Kuzmann[2], Alex Scrimshire[3], Paul A Bingham[3], Stjepko Krehula[4], Svetozar Musić[4],
5 Kazuhiko Akiyama[1], Shiro Kubuki[1]

6 **Title:** Photo-Fenton degradation of methylene blue using hematite-enriched slag under
7 visible light

8 **Affiliations and addresses of the authors:**

9 [1] Department of Chemistry, Graduate School of Science and Engineering, Tokyo
10 Metropolitan University, 1-1 Minami-Osawa, Hachi-Oji, Tokyo 192-0397, Japan

11 [2] Institute of Chemistry, Eötvös Loránd University, Pázmány P. s. 1/A, Budapest, 1117,
12 Hungary

13 [3] Materials and Engineering Research Institute, Faculty of Science, Technology and Arts,
14 Sheffield Hallam University, Howard Street, Sheffield S1 1WB, UK

15 [4] Division of Materials Chemistry, Ruđer Bosković Institute, Bijenička c. 54, 10000
16 Zagreb, Croatia

17 **E-mail address of the corresponding author:** Balasfora2000@yahoo.com

18
19
20

21

22

Photo-Fenton degradation of methylene blue using hematite-enriched slag under visible light

Ahmed S. Ali[1], Irfan Khan[1], Bofan Zhang[1], Kiyoshi Nomura[1], Zoltan Homonnay[2], Erno Kuzmann[2], Alex Scrimshire[3], Paul A Bingham[3], Stjepko Krehula[4], Svetozar Musić[4], Kazuhiko Akiyama[1], Shiro Kubuki[1]

[1] *Department of Chemistry, Graduate School of Science and Engineering, Tokyo Metropolitan University, 1-1 Minami-Osawa, Hachi-Oji, Tokyo 192-0397, Japan*

[2] *Institute of Chemistry, Eötvös Loránd University, Pázmány P. s. 1/A, Budapest, 1117, Hungary*

[3] *Materials and Engineering Research Institute, Faculty of Science, Technology and Arts, Sheffield Hallam University, Howard Street, Sheffield S1 1WB, UK*

[4] *Division of Materials Chemistry, Ruđer Bosković Institute, Bijenička c. 54, 10000 Zagreb, Croatia*

Abstract:

This study aims to find a suitable method to transform the amorphous iron oxides obtained from the incineration of combustible waste slag (CWS) into hematite. The resulting samples were utilized as heterogeneous photocatalysts for the photo-Fenton degradation of methylene blue (MB) aqueous solution. A good correlation was found between the MB degradation and the amount of hematite phase as confirmed by XRD and Mössbauer measurements. The largest rate constant (k) was $(4.1 \pm 0.08) \times 10^{-2}$ min^{-1} for MB decomposition under visible-light for the sample N5-50-800. The results are promising for both low-cost photocatalysts and recycling of combustible waste slags.

49 **Article highlights**

50 • A facile method for slag management into photocatalyst is presented
51 • The key component for degradation was the formation of hematite after heat-
52   treatment
53 • Hematite was confirmed using XRD and Mössbauer techniques
54

55 **Keywords** visible-light activated photocatalytic effect; photo-Fenton reaction; slag;

56   Hematite iron oxide; ^{57}Fe-Mössbauer spectroscopy

57

1. Introduction

59   Among many problems in our world today, two major problems grab the attention of

60 scientists and the public alike: combustible wastes, leading to scarcity of landfill and need

61 to find new recycling and circular economy approaches; and wastewater pollution. With

62 an increasing the world population, these two problems are becoming increasingly

63 serious unless more effective steps are taken [1].

64   For combustible wastes, many countries have established waste incineration or

65 waste-to-energy (WTE) plants to meet the lack of landfill whilst generating useful

66 energy, although the by-products from such processes (ashes and slags) can themselves

67 present both hazards and opportunities [2].

68   There are predominantly two types of slag; firstly, industrial slags which are

69 produced during ferrous and non-ferrous smelting processes. The smelting of copper,

70 lead and bauxite in non-ferrous smelting is designed to remove the iron and silica that

71 often occurs with those ores and separates them as iron-silicate-based slags [3]. On the

72 other hand, ferrous smelting in steel mills is designed to minimize iron loss so these slags

73 mainly consist of oxides of calcium, silicon, magnesium and aluminium. Secondly, there

74 are combustible waste slags (CWS) such as those produced by combustible waste

75 incineration and waste-to-energy (WTE) plants. Such wastes are incinerated at

76 temperatures of ca. 800°C, which reduces the volume to 1/20 of its original volume [4].

77   The compositions of CWS are similar to iron-containing silicate glasses, for which
78 the photocatalytic effect has previously been observed [5]. To date, CWS is used in civil
79 engineering works as a low-value base material or aggregate for the construction of roads
80 and concretes so new applications and new opportunities for valorization and recycling of
81 CWS is essential from both economic and environmental perspectives.

82   For wastewater, several techniques have been applied for the treatment of wastewater
83 effluents. Among these, photocatalysis is one of the most environmentally friendly
84 approaches. The most commonly-applied photocatalyst is TiO_2, which shows
85 photocatalytic activity under UV light due to its wide bandgap of 3.2 eV [6]. This wide
86 bandgap limits the practical uses of TiO_2 as UV light is only available from solar
87 irradiation as a small percentage, ca. 5%, compared to visible light, ca. 40% [7]. Iron
88 oxides, mainly hematite (Fe_2O_3) are promising alternatives due to their lower bandgap
89 around 2.3 eV, low cost, chemical stability and comparatively environmentally friendly
90 nature. Moreover, applying the Fenton reaction and the light-accelerated Fenton reaction,
91 commonly known as the photo-Fenton reaction, provides an added value for using iron
92 oxides as photocatalysts [8].

93   Iida   et   al.   [9]   reported   that   iron   alumino-silicate   glass,
94 $15Na_2O \cdot 15CaO \cdot 40Fe_2O_3 \cdot 11Al_2O_3 \cdot 19SiO_2$ (weight %), which has a similar composition
95 to CWS, showed a photocatalytic effect after heat treatment at 1000 °C for 100 min, with
96 a k (pseudo-first-order rate constant) of 9.26×10^{-3} min^{-1} for MB degradation. Ishikawa
97 et al. [5] reported that heat treatment of waste slag recycled glass-ceramics (WSRG) with
98 additional Fe_2O_3 content of 10, 30 and 50 mass% decomposed MB aqueous solution
99 with first-order rate constants (k) of 2.6, 2.3 and 2.7×10^{-3} min^{-1}, respectively, under
100 visible light irradiation. The degradation was related to the precipitated amount of α-
101 Fe_2O_3 nanoparticles. Khan et al. [10] also prepared iron-containing aluminosilicate glass
102 by a sol-gel method, which provided a k value of 8.61×10^{-2} min^{-1} in the photo-Fenton
103 degradation of MB, where the amount of precipitated hematite was increased by the
104 introduction of Al_2O_3.

105   In our previous work [11], we succeeded in preparing glass and glass-ceramics from
106 CWS by melt-quenching, obtaining k values of up to 2.2×10^{-2} min^{-1} by melting the slag
107 at 1400 °C, then subsequently heat treating it at 800 °C for 100 min. Here we aim to

108 enhance the results achieved by melt quenching by introducing a facile method for using

109 DSW as a photocatalytic material by treating as-collected DSW with HNO_3 and applying

110 the photo-Fenton reaction under visible light irradiation. The proposed method depends

111 on treating as-collected CWS with nitric acid at room temperature, which could further

112 reduce costs since no high preparation temperatures are required.

113   Reacting nitric acid with CWS compositions, which are mainly metal oxides, will

114 release the metals from the slag matrix in the form of nitrate salts. Iron oxide, Fe_2O_3, as

115 one of these oxides, will convert to iron nitrate which decomposes at high temperatures,

116 through a series of reactions, to form hematite, $\alpha\text{-}Fe_2O_3$ [12], one of the iron oxides used

117 as a visible-light photocatalyst. If some levels of $Fe(NO_3)_3$ persist after heat treatment, it

118 will increase the degradation [13]. There is little literature concerning the acid treatment

119 of CWS. Most related studies have used acid treatment for metals recovery from smelting

120 slags or for neutralizing the acid by adding basic slags. For example, Akcil et al. [14]

121 used nitric acid for the recovery of rare earth metals and production of precipitated silicon

122 dioxide from phosphorus slag which contains inorganic oxides similar to CWS. They

123 used concentrated nitric acid (7.0 − 7.5 M) and slag to acid ratio S: L = 1.0:2.6 at a

124 temperature of 90 °C for 1 hour. Nitric acid was also used for extracting soluble

125 phosphorus from slag with high P_2O_5 content by selective leaching. When nitric acid was

126 used, 66.8% of the solid solution was dissolved [15]. Some researchers have studied

127 photoactivity using metallurgical slag combined with TiO_2, CdO/graphene or other

128 materials, however, some drawbacks exist as some use UV light [16-18], long irradiation

129 times (e.g. 300 min) [19], or low pH (e.g. 3) [20].

130   In this work, the relationship between the visible-light activated catalytic effect and

131 local structure of the slag treated by nitric acid was, for the first time, investigated by

132 [57]Fe-Mössbauer spectroscopy, X-ray diffraction (XRD), transmission electron

133 microscopy (TEM) and optical absorption spectroscopy (UV-Vis).

134

135

136

137

138

2. Experimental Procedures

2.1. Materials

The slag used in this study was collected in July 2018 at the Tamagawa municipal waste combustion plant (Ohta-ku, Tokyo, Japan) according to the agreement between Tamagawa municipal waste combustion plant and faculty of science - Tokyo metropolitan university. Chemical reagents of Nitric acid HNO_3 (13M CAS No. 141-01361), hydrogen peroxide 30% (H_2O_2: CAS No. 081-04215) and methylene blue (MB: $C_{16}H_{18}N_3SCl_3 \cdot H_2O$, CAS No. 133-06962) were purchased from Wako, Japan.

2.2. Sample preparation

The as-collected slag was pulverized using an electric agate mortar and the XRF compositional analysis is presented in Table 1. As one of the important parameters affecting the dissolution rates, the ratio of slag/acid is very important [21], several ratios were prepared to study the effect of HNO_3 amount on the structure and photocatalytic ability. One gram of pulverized slag was added to different amounts (20, 10, 5 and 3 ml) of concentrated HNO_3 in a glass beaker and stirred at room temperature. The time required for full dissolution of the slag decreased with the amount of HNO_3. During the dissolution process, black orange fumes were liberated so the whole experiment was performed in an extraction hood. After the dissolution of the slag was complete, a green-coloured solution was obtained. The solution was then directly moved to a dryer at 80 °C in Petri dishes with thickness 2-3 mm, and held for 24 h. Over this period the colour changed from greenish to dark orange, consistent with the change in the iron oxide oxidation state from Fe^{2+} to Fe^{3+}, which was confirmed by ^{57}Fe Mössbauer measurements as shown in section 3.1.2. The dried samples were pulverized and heat-treated at 1000 °C according to the thermal gravimetric analysis (TG) results (see Fig. 1) at a heating rate of 5 °C/min and the resulting samples are thus denoted N20-1000, N10-1000, N5-1000 and N3-1000. For the samples prepared using dilute HNO_3, the same route was followed by adding additional amounts of distilled water as shown in Table 2. The preparation route is presented in scheme 1. The samples were denoted according to the percentage volume of

168   HNO_3 to the total volume of the solution and the heat treatment temperature. For

169   example, N5-75-800 means that for one gram of slag, the total volume of the solution is 5

170   ml while the HNO_3 volume is 75% and the heat treatment temperature is 800 °C. The

171   sample of 25% HNO_3 content did not fully dissolve so we obtained two samples, N5-75

172   and N5-50, which were heat-treated at 800 and 1000 °C.

173

2.3.   Characterization techniques

175   Sample structure before and after heat treatment were characterized by ^{57}Fe

176   Mössbauer spectroscopy, X-ray diffractometry (XRD), Scanning electron microscopy

177   (SEM), Transmission electron microscopy (TEM) and the Brunauer-Emmett-Teller

178   (BET) specific surface area analysis. ^{57}Fe Mössbauer spectra were measured using a

179   constant acceleration spectrometer. A source of 925 MBq ^{57}Co (Rh) was attached to an

180   MVT-1000 transducer connected to an MDU-1200 drive unit. The drive unit was

181   connected to a DFG-1200 digital function generator with 1200 channels. Transmitted γ-

182   rays were detected by a proportional counter. The signals were amplified by an ORTEC

183   142 preamplifier. The applied voltage (2 kV) was obtained by using an ORTEC 556 High

184   voltage–power supply, and an ORTEC 570 amplifier. The amplified signals were

185   monitored with a PC via an ORTEC EASYMSC. Samples with weight = 40 mg were

186   homogeneously dispersed in a circular sample holder with 10 mm diameter; inserted into

187   the spectrometer, and measured until the total counts collected were greater than 10^6.

188   Isomer shifts are given relative to α-Fe, which was measured as a reference. The

189   Mösswinn 3.0i XP software was used to analyze the obtained spectra. XRD patterns were

190   recorded using a RINT TTR3, Rigaku diffractometer between 2θ of 10° to 80°, with

191   precision and scan rates of 0.02 and 5°/ min, respectively. Cu-Kα X-rays ($\lambda = 0.1541$ nm)

192   were generated at 50 kV and 300 mA, and monochromated. SEM images were taken by

193   Keyence VE 9800 with the applied voltage of 2 kV, and magnification of 2000x. TEM

194   images were obtained using a JEM-3200FS Field Emission Energy Filter Electron

195   Microscope. The Brunauer-Emmett-Teller (BET) specific surface area was estimated

196   from N_2 isotherms obtained using a BELSORP mini II (BEL Japan, Osaka, Japan) at 77

197   K. The analyzed samples were evacuated at 573 K for 3 h before each measurement.

198

2.4.   Photo-Fenton Reaction

199

200   For the evaluation of photocatalytic properties, we used 40 mg of pulverized sample

201   and 10 mL of methylene blue aqueous solution (MB_{aq}) with an initial concentration of

202   20 μmol L^{-1}. Additional amounts of hydrogen peroxide (9.79 M) (Wako: 081-04215 30%

203   mass/mass) was added to the MB solution. UV–Vis optical absorption spectra of the MB

204   solution before and after the photocatalytic reaction test were measured from the

205   absorbance of the peak at 665 nm, using a GENESYS™ 10S UV-Vis spectrophotometer.

206   The light was emitted by a metal-halide lamp with output wavelengths from 420 to

207   750 nm, an output power of 100 W and an intensity of 6 mW cm^{-2}, with the distance

208   between the sample and the light source maintained at 20 cm, and a UV filter was used.

209   All samples were also measured in the dark to investigate the effect of adsorption as a

210   control. All measurements were performed at room temperature.

211

3. Results and discussion

212

3.1.   Structural characterization

213

3.1.1 XRD

214

215   Figure 2(a) shows the XRD patterns for the samples dissolved in concentrated HNO_3

216   heat-treated at 1000 °C for 100 min. The samples N20, N10 and N5 show crystalline

217   peaks ascribed to hematite (Fe_2O_3, PDF No. 01-089-0598), gehlenite (Ca_2Al (Al Si) O_7,

218   PDF No. 01-089-5917) and esseneite ($CaFe_{0.6}Al_{1.34}Si_{1.08}O_6$, PDF No. 01-084-1206). The

219   sample N3 does not evidence peaks related to hematite but shows peaks consistent with

220   gehlenite and esseneite, with the same PDF numbers previously mentioned. This sample

221   also produces diffraction peaks attributed to Andradite ($Ca_3Fe_2O_{12}Si_3$, PDF No. 01-084-

222   1206). The intensity of hematite peaks decreases, with decreasing HNO_3 addition from 20

223   to 5 ml for the samples N20 to N5, respectively. These results indicate that the amount of

224   HNO_3 has a large impact on the development of the hematite phase obtained from heat-

225   treatment. Since hematite is known as a visible light photocatalyst, it was expected that

226   the sample N20 would produce the highest MB_{aq} degradation values due to the existence

227   of hematite as the most prominent phase. It was also expected that the MB_{aq} degradation

228   of the samples N10, N5 and N3 would decrease gradually due to the gradual decrease in

229   hematite content. It should be noted that in our previous work [11], we could not detect

230   any XRD peaks related to hematite in the slag after melting at 1400 °C and heat-

231   treatment at 800 °C for 100 min unless Fe_2O_3 additions were made to increase the Fe_2O_3

232   content of the resulting material to 50%. Figure 2(c) shows the XRD pattern of the slag

233   (same slag used in this study), melted at 1400 °C and heat-treated at 800 °C for 100 min.

234   The identified phases are iron silicon oxide ($Fe_{2.95}Si_{0.05}O_4$, PDF No. 00-052-1140) and

235   calcium silicate (Ca_2SiO_4, PDF No. 00-024-0234). This means that dissolving the slag in

236   HNO_3 can produce hematite without the requirement for additional Fe_2O_3, leading to

237   better degradation results and simpler production.

238   Figure 2(b) shows the XRD patterns for the samples dissolved in dilute HNO_3 (75

239   and 50%) after heat treatment at 800 and 1000 °C for 100 min, respectively. Clear

240   diffraction peaks can be detected for gehlenite (Ca_2Al (Al, Si) O_7, PDF No. 01-089-

241   5917), hematite (Fe_2O_3, PDF No. 01-089-0596) and andradite (Ca_3Fe_2 (SiO_4)$_3$, PDF No.

242   01-084-1935) for all samples. Heat treatment at 1000 °C for both N5-75 and N5-50

243   samples increased their crystallinity as demonstrated by the narrower diffraction peaks

244   compared to those obtained in the corresponding samples heat-treated at 800 °C,

245   suggesting that the crystallite size increased as the temperature increased, which is also

246   reflected in the measured surface area. Also, the intensity of hematite peaks decreased

247   while the intensity of gehlenite peaks increased for heat treatment at 1000 °C compared

248   to 800 °C. It is thus concluded that HNO_3 concentration plays a major role in controlling

249   the obtained phases while heat treatment temperature affects the phase distribution and

250   the crystallite size. These results are consistent with that obtained from Mössbauer

251   spectra.

252

253   3.1.2 Mössbauer Spectroscopy

254   3.1.2.1 Mössbauer spectroscopy of slag dissolved in concentrated HNO_3

255   The as-collected slag spectra and fitted data, in Fig. 4(c) and Table 3, show two

256   paramagnetic doublets with δ = 1.01 $\pm$ 0.01 mm s^{-1} and 0.48 $\pm$ 0.06 mm s^{-1} related to

257   Fe^{II} O_h and Fe^{III} O_h, respectively. The spectra and parameters for all samples prepared

258   using concentrated HNO_3 after heat treatment at 1000 °C for 100 min are shown in Fig. 3

259   and Table 3, respectively. The spectra of the samples N20, N10 and N5 exhibit two

260   doublets related to Fe^{III} and one sextet related to hematite. The sample N3 shows only

261   two doublets with $\delta = 0.29 \pm 0.01$ and 0.38 ± 0.01 mm s^{-1} related to Fe^{III} T_d and Fe^{III} O_h,

262   respectively. These results show that Fe^{II} in the slag was oxidized to Fe^{III} upon dissolution

263   in HNO_3 and drying, while hematite can be formed by heat treatment. On the other hand,

264   the spectra and fitted parameters for the sample prepared by melt-quenching after heat

265   treatment at 800 °C for 100 min, shown in Fig. 4(c) and Table 3, show two doublets with

266    $\delta = 0.36 \pm 0.01$ and 0.34 ± 0.01 mm s^{-1}, related to Fe^{III} O_h, which is similar to

267    $\delta = 0.38 \pm 0.04$ mm s^{-1} obtained for the sample prepared by melt-quenching reported in

268   our previous paper [11]. The detection of hematite in the dissolved slag following heat

269   treatment is interesting behaviour compared to melt-quenching, although both samples

270   have the same total iron content. In our previous paper [11], where the samples were

271   prepared using melt-quenching, hematite was detected by RT-Mössbauer only for the

272   sample containing 50% Fe_2O_3. The existence of hematite in the dissolved slag was found

273   to be effective for MB degradation, as will be discussed in degradation measurements

274   section. This demonstrates the advantage of dissolving slag in HNO_3 over melt-

275   quenching, to prepare an effective, low-cost photocatalyst. It is noticed that the hematite

276   absorption peak decreases as the amount of HNO_3 decreased, where it was 33, 29 and

277   20% for N20, N10 and N5, respectively. This may be due to the lower amount of HNO_3

278   resulting in the incomplete dissolution of iron oxide in slag. As a result, a lower amount

279   of iron nitrate may be formed, and consequently, the hematite, which results from thermal

280   decomposition of iron nitrate, was decreased. This can be seen in the case of sample N3,

281   for which no hematite was detected for the above-mentioned reason. The Mössbauer

282   results are consistent with the XRD results.

283

284   **3.1.2.2 Mössbauer spectroscopy of slag dissolved in diluted HNO_3**

285   The spectra and fitted parameters for the samples dissolved in dilute HNO_3 (75 and

286   50%) before and after heat treatment at 800 and 1000 °C for 100 min are shown in Fig.

287   4(a), (b) and Table 4, respectively. Using diluted HNO_3 (with HNO_3 of 75%) resulted in

288   hematite content with absorption peaks of 38 and 40% for the samples N5-75-1000 and

289   N5-75-800 °C, respectively. Further decrease in HNO_3 concentration to 50% resulted in

290   more hematite with absorption peaks of 33 and 50% for the samples N5-50-1000 and N5-

291   50-800 °C, respectively. Compared to the hematite content (20%) in the case of the

292   sample produced using concentrated HNO_3 (N5-1000), it can be observed that more

293   dilute HNO_3 is more effective for obtaining high hematite contents in the final materials,

294   which can enhance the photocatalyst performance. This can be explained by the

295   hydrolysis being affected by the ratio of water in the solution. Before heat treatment, both

296   samples show two doublets related to $Fe^{III} O_h$ with $\delta = 0.37 \pm 0.02$ and 0.57 ± 0.04

297    $mm\ s^{-1}$ for N5-75, $\delta = 0.36 \pm 0.01$ and 0.39 ± 0.05 $mm\ s^{-1}$ for N5-50, respectively,

298   indicating the oxidation of Fe^{II} in the slag to Fe^{III} after drying, however, heat treatment is

299   required for the formation of hematite. To obtain more investigation about the effect of

300   heat treatment temperature on the obtained hematite, the sample N5-50 was heat-treated

301   at 600 °C for 100 min. From Mössbauer measurements shown in Fig 4(c) and Table 4,

302   only two doublets were obtained with $\delta = 0.32 \pm 0.01$ and 0.35 ± 0.02 $mm\ s^{-1}$ and

303   assigned as $Fe^{III} T_d$ and $Fe^{III} O_h$, respectively, with no hematite detected. These results

304   show that, of those temperatures studied here, the most effective heat treatment

305   temperature to obtain hematite is 800 °C.

306

307   3.1.3. Morphology

308   Fig. 5 (A, B) show the SEM and TEM images of the samples N5-75 and N5-50 heat-

309   treated at 800 and 1000 °C, respectively. From SEM images, all samples show uneven

310   surfaces with different sizes and morphologies. The size and morphology are smaller,

311   more porous and uniform in the case of lower heat-treated samples N5-75-800 and N5-

312   50-800 compared to higher heat-treated samples N5-75-1000 and N5-50-1000. The

313   average aggregate' sizes are 4.2, 5.4, 3.9, and 4.4 µm for N5-75-800, N5-75-1000, N5-50-

314   800 and N5-50-1000, respectively. Average aggregate' sizes are lower in the case of

315   lower heat-treatment which is an advantage for using these samples in practical

316   applications. The TEM images give a more clear analysis of these samples, for which the

317   particle size for N5-75-800 varies from 5 to 9 nm, having the smallest particle size among
318   all samples studied. For sample N5-75-1000, the particle size has grown slightly to
319   approximately 12 nm. The sample N5-50-800 has particles with a size approximately 21
320   nm while sample N5-50-1000 exhibits particles with sizes varies from 15 to 24 nm.
321   These larger particle sizes for samples heat-treated at 1000 °C are consistent with their
322   higher heat treatment temperatures.
323

3.2.   Photocatalytic properties

3.2.1. Photo-Fenton reaction for the concentrated HNO_3 treated samples

327   The results of MB degradation under the photo-Fenton reaction of the heat-treated
328   samples N20, N10, N5 and N3 (see Fig. 6) show that the degradation and *k* values
329   increase with the amount of HNO_3 used for dissolving the slag. This trend can be
330   explained by considering the structural characterization from both XRD and Mössbauer
331   spectroscopy; it is correlated with the amount of hematite in the sample. The apparent *k*
332   values for the samples N20, N10, N5 and N3 were $(8.1 \pm 0.2, 5.0 \pm 0.2, 3.0 \pm 0.1$ and
333   $1.4 \pm 0.1) \times 10^{-2}$ min^{-1} after 60 min of irradiation where the hematite contents were 33%,
334   29%, 20% and zero, respectively. To clarify the greater effectiveness of this method over
335   melt-quenching, another sample was prepared by melt-quenching using the same
336   collected slag, and then heat-treated at 800 °C for 100 min. The MB test for this sample
337   resulted in a *k* value of $2.2 \pm 0.1 \times 10^{-2}$ min^{-1} after 3h of irradiation. These results show
338   that the acid dissolution and heat treatment method resulted in cost-effective visible light
339   photocatalysts also reducing the time required for the MB degradation from 3h to 1h. The
340   degradation of the blank sample (without catalyst) and dark samples (measured in the
341   dark) have small *k* values of $(0.25 \pm 0.01, 0.28 \pm 0.01, 0.25 \pm 0.01, 0.21 \pm 0.01,$ and
342   $0.10 \pm 0.01) \times 10^{-2}$ min^{-1}, respectively, which means that the degradation is due mainly to
343   photoactivity rather than photolysis or adsorption. The advantage of the photo-Fenton
344   reaction over photoactivity can be clarified by measuring all samples under the same
345   conditions without applying the photo-Fenton reaction. The *k* values for samples N20,
346   N10, N5 and N3 were $(1.32 \pm 0.03, 1.01 \pm 0.02, 0.48 \pm 0.01$ and $0.3 \pm 0.01) \times 10^{-2}$ min^{-1},

347 respectively, which are far smaller compared to k values from the photo-Fenton reaction,

348 however, it has the same trend in variation of k as a function of hematite content.

349

350

3.2.2. Photo-Fenton reaction for the diluted HNO$_3$ treated samples

352 We aimed to prepare a cost-effective catalyst so the k / acid ratio was calculated to

353 choose the most practical sample. From these results, shown in Fig. 6 inset, sample N5

354 was chosen since it provided the highest k / acid ratio. The amount of HNO$_3$ was diluted

355 with distilled water to 75, 50 and 25%. The slag could not be fully dissolved at the low

356 HNO$_3$ concentration of 25% so two samples denoted as N5-75 and N5-50 were obtained

357 for the corresponding HNO$_3$ concentrations of 75 and 50%, respectively. Both samples

358 were heat-treated at 1000 and 800 °C according to the TG results (see Fig. 1) and denoted

359 as samples N5-75-1000, N5-75-800, N5-50-1000 and N5-50-800, respectively. The

360 photo-Fenton measurements for these samples are shown in Fig. 7, and the results can be

361 summarized as follows:

362 Firstly, the k values in the case of samples N5-75-1000 and N5-75-800 were

363 $(3.9 \pm 0.1$ and $4.5 \pm 0.1) \times 10^{-2}$ min^{-1}, respectively, while for samples N5-50-1000 and

364 N5-50-800 it was $(3.4 \pm 0.1$ and $4.1 \pm 0.1) \times 10^{-2}$ min^{-1}, respectively. The higher k values

365 in the case of higher acid content indicate that the slag / acid ratio plays a major role in

366 the effectiveness of the prepared catalyst.

367 Secondly, the results of photo-Fenton reactions are correlated with the hematite

368 content of the sample. The Mössbauer absorption area (Table 4) for sample N5-50-800

369 was detected to be 50%, having a k value of $(4.1 \pm 0.1) \times 10^{-2}$ min^{-1} while absorption area

370 was 33% for sample N5-50-1000 with a lower k value of $(3.9 \pm 0.1) \times 10^{-2}$ min^{-1}. The

371 same trend can be observed for the sample N5-75 although the difference in the

372 absorption area is not large (40% for 800 °C and 38% for 1000 °C) but it is also

373 important to consider the additional doublet for the sample prepared at 800 °C with the

374 octahedral site and absorption area of 10%.

375 Thirdly, for each sample, it can be seen that the lower heat treatment temperature

376 resulted in higher MB degradation. This can be an indication of particle size (and

377   therefore higher surface area) contribution where the particle size is larger in the higher

378   temperature samples. From XRD shown in Fig. 2(a) and (b), it can be observed that both

379   samples N5-75-1000 and N5-50-1000 produce sharp diffraction peaks with narrow full-

380   width, half-maximum (FWHM) line widths compared to XRD patterns for samples N5-

381   75-800 and N5-50-800. Sharp diffraction peaks correspond to larger crystallite size,

382   which is reflected in the surface area, an important parameter for effective photocatalysts.

383   To clarify the contribution of surface area and its relation to MB degradation, the surface

384   areas of these samples were measured. The BET results (Table 5) clearly show that the

385   surface area has a positive correlation with MB degradation, where it is larger in the case

386   of higher HNO_3 content and low heat treatment temperature, (3.64 and 5.38 m^2 / g) for

387   samples N5-75-1000 and N5-75-800 compared to the lower HNO_3 content (2.16 and 2.63

388   m^2 / g) for samples N5-50-1000 and N5-50-800, respectively.

389   Fourthly, the sample prepared by melt-quenching has a *k* value of $(2.2 \pm 0.1) \times 10^{-2}$

390   min^{-1} which is almost half of that for the HNO_3 produced samples. By considering the

391   structural analysis of this sample, it can be seen that it produces only Mössbauer doublets

392   and no hematite sextets, and thus no hematite can be observed by either XRD Fig. 2(c) or

393   Mössbauer spectroscopy Fig. 4(c). This may be the reason for the low *k* value obtained

394   for this sample in addition to the fact that the melt-quenching method results in lower

395   surface area.

396   Fifthly, before heat treatment, the photoactivity of both samples N5-75 and N5-50

397   were measured. It was found that they produce much higher MB degradation than the

398   heat-treated samples, with 88% of MB removal for both samples after only 20 min. Both

399   samples were measured in dark conditions and also provide high MB degradation of 68%

400   and 61% after 20 min for samples N5-75 and N5-50, respectively. These values were

401   mainly due to the effect of adsorption and homogeneous Fenton reaction rather than the

402   photo-Fenton reaction. Iron nitrate salts (present in the samples before heat treatment)

403   accompanied by low pH (due to the presence of HNO_3 which is not completely removed

404   after drying at 80 °C) are a good environment for the homogeneous Fenton reaction. The

405   sample N5-50 was heat-treated at 600 °C for 100 min and shows a lower *k* value of

406     $(1.5 \pm 0.1) \times 10^{-2}$ min^{-1} compared to sample N-5-50-800. By considering the fitted

407   Mössbauer parameters for this sample (Table 4), the spectra are composed of two

408   doublets with $\delta = (0.35 \pm 0.02$ and $0.32 \pm 0.01)$ mm s^{-1} assigned as Fe^{III} O_h and Fe^{III} T_d,

409   respectively, where hematite is not detected (lack of sextet), which confirms that hematite

410   plays the major role in the MB degradation and it can be obtained only by heat treatment

411   at 800 °C.

412

413   3.2.3. Parameters affecting MB degradation

414   The sample N5-50-800 has lower acid content and lower heat treatment temperature,

415   hence, it was chosen for further study.

416

417   a- Effect of H$_2$O$_2$

418   The oxidation of organic pollutants using Fenton reactions is strongly dependent on

419   the addition of H$_2$O$_2$ because it controls the generation of active radicals. The MB

420   degradation has been studied under a range of H$_2$O$_2$ concentrations (0.1 to 1.6 M); the

421   results are shown in Fig. 8(a). By increasing the H$_2$O$_2$ concentration from 0.1 to 0.35 M

422   the degradation increases from 70.3% to 90.6% removal of MB where more H$_2$O$_2$

423   produces more active radicals [22]. However, excess H$_2$O$_2$ decreases the degradation

424   from 90.6% to 80.8%, mostly because it acts as a scavenger of hydroxyl radicals [22, 23].

425   Also, more H$_2$O$_2$ can generate more$^.$OH, which can be dimerized to form H$_2$O$_2$ so

426   cumulative effects can inhibit the MB degradation. The excess of H$_2$O$_2$ may also

427   encourage the formation of less active hydroperoxyl radicals which can react with

428   hydroxyl radicals to form water [24]. The best-performing H$_2$O$_2$ concentration was found

429   to be 0.35 M, which produced a k value of 4.1×10^{-2} min^{-1}.

430

431   b- Effect of MB concentration

432   Dye concentration affects the intensity of light passing through the reaction medium

433   to reach the surface of the photocatalyst. The photodegradation of MB was conducted

434   under initial concentrations of 20, 40 and 60 μM. MB degradation is shown in Fig. 8(b)

435   and displays an inverse relation with the initial concentration, where it was 90.6%, 69.2%

436   and 65.5% for MB of 20, 40 and 60 μM after 60 min of irradiation, respectively. This can

437 be attributed to the decrease in˙OH, radical generation due to the coverage of catalyst

438 active sites by the adsorbed dye [24, 25]. Moreover, the intermediate compounds formed

439 during the degradation process increase with the increase in the initial dye concentration

440 and might consume some active radicals that are supposed to react with the dye

441 molecules [26].

442

443 **c- Effect of catalyst loading**

444 Determining the optimum catalyst loading is essential in photodegradation reactions,

445 since it helps in consequently scaling up the photocatalytic process, thereby affecting the

446 economics of the whole process. This includes the production cost which should be

447 minimized. Not only this but also catalyst recovery after the end of the reaction must be

448 considered. In our case, the prepared catalyst (iron silicate powder) loading was varied

449 from 2 to 24 g L^{-1}. The results of MB degradation measured after 60 min as a function of

450 the catalyst loading are presented in Fig. 8(c). Increase in the MB degradation was

451 observed, from 84.4% for 2 g L^{-1} to 90.6% for 4 g L^{-1}. This increase in degradation is due

452 to the increase in the active surfaces for the same unit volume of MB [24], which will

453 lead to an increase in the absorbed photons and consequently in the generation of˙OH

454 radicals which initiate the reaction [25]. Further increase leads to a decrease in MB

455 degradation from 90.6% for 4 g L^{-1} to 81.8% for 24 g L^{-1}, mostly caused by a reduction in

456 light intensity as the solution opacity increases [27, 28]. It is also possible that at higher

457 catalyst loading, the iron act as a scavenger and reacts with˙OH radicals [24]. The

458 optimum catalyst loading was found to be 4 g L^{-1}.

459

460 **d- Effect of temperature**

461 The reaction temperature is a critical operating parameter. Fig 8(d) shows the

462 influence of the reaction temperature on MB removal. The experiments were performed

463 at four different temperatures, namely, 303K, 313K, 323K, and 333K. It can be seen that

464 with increasing temperature, the rate of the reaction increases from 4.1×10^{-2} min^{-1} at

465 303K to 13.0×10^{-2} min^{-1} at 333K. The increase in temperature increases interaction of

466　the hydroxyl radicals and the dye molecules and the reaction competes more efficiently

467　with electron-hole recombination [11, 28].

468　　The activation energy (E_a), estimated using the rate constants (k_t) from the Arrhenius

469　equation [22], were calculated according to Eq. (1)

470

471　$$\ln k_t = -E_a/RT + \ln A \qquad (1)$$

472

473　Where k_t is the reaction rate constant as a function of temperature; E_a ($J \cdot mol^{-1}$) is the

474　apparent activation energy; R is the universal gas constant of 8.314 $J \cdot mol^{-1} \cdot L^{-1}$; T (K) is

475　the absolute temperature; A is the Arrhenius pre-exponential factor

476　　The apparent activation energy of MB obtained in this study Fig. 8(d) (inset) was

477　31.5 $KJ.mol^{-1}$ which is higher than values obtained from other studies reported by

478　Okamoto [29] for the photodegradation of phenol (10.0 kJ / mole) and by Al-Sayyed [30]

479　for the degradation of 4-chlorophenol (5.4 kJ / mole). The high value obtained in this

480　study suggests that thermal activation is important to accelerate the photo-degradation

481　[31].

482

483　**e-　Effect of pH**

484

485　　The pH is considered the main parameter affecting the adsorption/desorption

486　processes due to its impact on the surface charge of the catalyst. This affects the

487　adsorption of reactants and dye molecules on the surface of the catalyst, and desorption

488　of the reaction products back into solution [26]. The effect of the solution pH within the

489　range of 3 to 11 on the degradation efficiency was investigated; the results are presented

490　in Fig. 9. An increase in the degradation efficiency was observed with increasing pH

491　from 3 to 11. At pH 11 the MB degradation is highest at 93.8% in 20 min, while the

492　maximum degradation at lower pH was 32.2% and 80.5 % for pH of 9 after 20 and 60

493　min, respectively. The pH of the solution can enhance the degradation and ensure strong

494　adhesion of dye molecules on the surface of the catalyst. This depends on the nature of

495   the dye (cationic, anionic or neutral). In our case, MB, which is a cationic dye, will be

496   adsorbed more quickly at higher pH and consequently, an increase in the MB degradation

497   rate is expected [25, 26]. The alkaline medium can also facilitate the formation of $^-$OH

498   ions which are responsible for the generation of $^.$OH radicals; this will lead to an increase

499   in photodegradation rate [32]. It was reported that in acidic solutions, the surfaces of

500   photocatalysts are positively charged while they are negatively charged in alkaline

501   solutions [33]. As a result, the efficiency of MB photodegradation is expected to increase

502   with pH, owing to electrostatic interactions between the negative surface and the MB

503   cations.

504   To understand the influence of the solution pH on the Fenton process, the point of

505   zero charge (PZC) of the N-5-50-800 sample was estimated (Inset Fig. 9). The obtained

506   PZC value of 10.6 suggests that the surfaces of the catalyst were negatively charged at

507   pH higher than 10.6, which is ideal for the degradation of the cationic MB due to

508   electrostatic interactions [22]. The high value of PZC explains the rapid increase in the

509   degradation from 32.2% to 93.8% for pH of 11 and 9 after 20 min, respectively.

510

511   3.2.4. Stability and Recyclability

512   Catalyst recyclability is an increasingly important feature of catalysts for industrial

513   applications. In this study, the reusability of the best-performing sample, N5-50-800, was

514   tested at an initial pH of 11. Fig. 10 illustrates the relationship between MB degradation

515   efficiency and the number of cycles, tested at 20 min of irradiation after 7 successive

516   cycles where the degradation was decreased by only 6.3%. The repeated measurements

517   were carried out by centrifuging the solution followed by removing and replacing it with

518   a new MB solution. No further filtration or drying of the powder was carried out between

519   subsequent experiments, which can further lower the operational cost if the catalyst were

520   applied in a large-scale process.

521

522   Conclusions

523   A visible light photocatalyst was successfully prepared by dissolving the combustible

524   waste slag in nitric acid. The photocatalytic activity of the prepared samples was found to

525 obey the pseudo-first-order rate constant, having a k-value of $(4.1 \pm 0.1) \times 10^{-2}$ min^{-1} for
526 sample N5-50-800 in the photo-Fenton process. The k-value increased to
527 $(1.4 \pm 0.1) \times 10^{-1}$ min^{-1} for the same sample after controlling the initial pH to 11. The
528 sample prepared by the melt-quenching method using the same slag has a maximum k
529 value of $(2.2 \pm 0.1) \times 10^{-2}$ min^{-1} under the same conditions, which illustrates the
530 effectiveness of the method used in this study. The obtained results of photocatalytic
531 activity are correlated to the amount of hematite in each sample, as detected by XRD and
532 ^{57}Fe Mössbauer measurements. It was found that the HNO$_3$ concentration and heat
533 treatment temperature have a large impact on both hematite content and the surface area
534 of the prepared samples and, consequently, on the methylene blue degradation ability.
535 The optimum conditions for practical usage of the samples are using sample N5-50-800
536 in the photo-Fenton reaction with 0.35 M of H$_2$O$_2$, a catalyst (iron silicate powder)
537 loading of 4 g L^{-1}, MB initial concentration 20 μM and initial pH of 11.

538 **CRediT author statement:**

545

Declaration on conflict of interests

547 The authors declare that they have no known competing financial interests or personal
548 relationships that could have appeared to influence the work reported in this paper.

Acknowledgements

554

References

[1] Ferronato N, Torretta V (2019) Waste mismanagement in developing countries: A review of global issues. Int. J. Environ. Res. Public Health 16:1–28

[2] Mary Joseph A, Snellings R, Heede P V d, Matthys S, Belie N.D (2018) The use of municipal solid waste incineration ash in various building materials: A Belgian point of view. Materials 11:1–30

[3] Yildirim I Z, Prezzi M (2011) Chemical, mineralogical and morphological properties of steel slag. Adv. Civ. Eng. 2011:1–13

[4] Perrot J F, Alison Subiantoro A (2018) Municipal waste management strategy review and waste-to-energy potentials in New Zealand. Sustainability 10:1–12

[5] Ishikawa S, Kobzi B, Sunakawa K, Nemeth S, Lengyel A, Kuzmann E, Homonnay Z, Nishida T, Kubuki S (2017) Visible-light activated photocatalytic effect of glass and glass ceramic prepared by recycling waste slag with hematite. Pure Appl. Chem. 89: 535–554

[6] Fujishima A, Honda K (1972) Electrochemical photolysis of water at a semiconductor electrode. Nature 238:37-38

[7] Koehl M, Philipp D, Lenck N, Zundel M (2009) Development and application of a UV light source for PV-module testing. Proc. of SPIE 7412:1–7

[8] Aramyan S, Moussavi M (2017) Advances in Fenton and Fenton Based Oxidation Processes for Industrial Effluent Contaminants Control-A Review. Int. J Environ. Sci. Nat. Res. 2:1–18

[9] Iida Y, Akiyama K, Kobzi B, Sinkó K, Homonnay Z, Kuzmann E, Ristić M, Krehula S, Nishida T, Kubuki S (2015) Structural analysis and visible light-activated photocatalytic activity of iron-containing soda lime aluminosilicate glass. J. Alloys. Comp. 645:1–6

[10] Khan I, Nomura K, Kuzmann E, Homonnay Z, Sinkó K, Ristić M, Krehula S, Musić S, Kubuki S (2020) Photo-Fenton catalytic ability of iron-containing aluminosilicate glass prepared by sol-gel method. J. Alloys. Comp. 816:1–7

583 [11] Ali A S, Nomura K, Homonnay Z, Kuzmann E, Scrimshire A, Bingham P A,
584   Krehula S, Ristić M, Musić S, Kubuki S (2019) The relationship between local
585   structure and photo‑ Fenton catalytic ability of glasses and glass‑ ceramics prepared
586   from Japanese slag. J. Radioanal. Nuc. Chem. 322:751–761

587 [12] Melnikov P, Nascimento V A, Arkhangelsky I V, Zanoni Consolo L Z, de Oliveira L
588   C S (2014) Thermal decomposition mechanism of iron (III) nitrate and
589   characterization of intermediate products by the technique of computerized
590   modeling. J Therm. Anal. Calorim. 115:145–151

591 [13] Machulek A, Quina F, Gozzi F, Silva V, Friedrich L, Moraes J (2012) In: Puzyn T
592   (ed) Organic pollutants ten years after the Stockholm convention—environmental
593   and analytical update, 1st edn. Intechopen, London

594 [14] Akcil A, Karshigina Z B, Bochevskaya Ye G, Abisheva Z S (2018) Conditions of
595   nitric acid treatment of phosphorus slag from REMs recovery and production of
596   precipitated silicon. Metallurgy 2:28–38

597 [15] Du C, Gao X, Ueda S, Kitamura S (2016) Effects of Cooling Rate and Acid on
598   Extracting Soluble Phosphorus from Slag with High P_2O_5 Content by Selective
599   Leaching. ISIJ International 510:1–10

600 [16] Zhang Y, He P. Chen H (2018) A novel CdO/graphene alkali-activated steel slag
601   nanocomposite for photocatalytic degradation of dye wastewater. Ferroelectrics
602   522:1–8

603 [17] Kang L, Zhang Y, Wang L, Zhang L, Zhang K, Liu L (2015) Alkali-Activated steel
604   slag-based besoporous material as a new photocatalyst for degradation of dye from
605   wastewater. Integr. Ferroelectr. 162:8–17

606 [18] Zeynolabedin R, Mahanpoor K (2017) Preparation and characterization of nano-
607   spherical $CoFe_2O_4$ supported on copper slag as a catalyst for photocatalytic
608   degradation of 2-nitrophenol in water. J. Nanostruct. Chem. 7:67–74

609 [19] Salgado S Y A, Pérez A A M, López M S, Zamora R M R (2016) Evaluation of
610   metallurgical slag as a Fenton-type photocatalyst for the degradation of an
611   emerging pulutent: Diclofenac. Catal. Today 266:126–135

612 [20] Gong X, Jia F, Liu R, Ye F, Guan H, Wang R, Guo G (2014) Study on preparation
613   and photocatalytic activity of photocatalyst made from Ti-bearing blast furnace slag.
614   Appl. Mech. Mater. 526:33–39

615 [21] Sun Y, Zhang J, Wang Y, Li Q (2016) Inhibitory Effect of Thioacetamide On CdS
616   Dissolution During Photocatalytic Oxidation of 2,4-Dichlorophenol. Rare Metal
617   Technology 1:87-88

618 [22] Saleh R, Taufik A (2019) Degradation of methylene blue and congo-red dyes using
619   Fenton, photoFenton, sono-Fenton, and sonophoto-Fenton methods in the presence
620   of iron (II,III) oxide/zinc oxide/graphene (Fe_3O_4/ZnO/graphene) composites. Sep.
621   Purif. Technol. 210:563-573

622 [23] Guo S, Zhang G, Wang J (2014) Photo-Fenton degradation of Rhodamine B using
623   Fe_2O_3–Kaolin as heterogeneous catalyst: Characterization, process optimization
624   and mechanism. J. Colloid Interf. Sci. 433:1-8

625 [24] Nasuh N, Ismail S, Hameed H (2016) Activated electric arc furnace slag as an
626   effective and reusable Fenton-like catalyst for the photodegradation of methylene
627   blue and acid blue 29. J. Taiwan Inst. Chem. E. 67:235–243

628 [25] Reza K M, Kurny A S W, Gulshan F (2017) Parameters affecting the photocatalytic
629   degradation of dyes using TiO_2: a review. Appl. Water Sci. 7:1569–1578

630 [26] Abdellah M H, Nosier S A, El-shazly A H, Mubarak A A (2018) Photocatalytic
631   decolorization of methylene blue using TiO_2/UV system enhanced by air sparging.
632   Alex. Eng. J. 57:3727–3735

633 [27] Soltani N, Saion E, Hussein M Z, Erfani M, Abedini A, Bahmanrokh G, Navasery
634   M, Vaziri P (2012) Visible light-induced degradation of methylene blue in the
635   presence of photocatalytic ZnS and CdS nanoparticles. Int. J. Mol. Sci., 13:12242–
636   12258

637 [28] Gajbhiye S B (2012) Photocatalytic degradation study of methylene blue solutions
638   and its application to dye industry effluent. IJMER 2:1204–1208

639 [29] Okamoto K, Yamamoto Y, Tanaka H, Tanaka M, Itaya A (1985) Heterogeneous
640   Photocatalytic Decomposition of Phenol over TiO_2 Powder. Bull. Chem. Soc. Jpn.
641   58: 2015-2022

642　[30] Al-Sayyed G, D'Oliveira J, Pichat P (1991) Semiconductor-sensitized
643　　　　photodegradation of 4-chlorophenol in water. J. Photochem. Photobiol. A: Chem. 58:
644　　　　99–114

645　[31] Hu Q, Liu B, Zhang Z, Song M, Zhao X (2014) Temperature effect on the
646　　　　photoeatalytic degradation of methyl orange under UV-vis Light irradiation. Journal
647　　　　of Wuhan University of Technology-Mater. Sci. Ed. 25:210-213

648　[32] Kaur J, Bansal S, Singhal S (2013) Photocatalytic degradation of methyl orange
649　　　　using ZnO nanopowders synthesized via thermal decomposition of oxalate precursor
650　　　　method. Physica, B Condens. Matter 416:33–38

651　[33] Tang Z W, Huang C P (1995) Inhibitory Effect of Thioacetamide on CdS
652　　　　Dissolution During Photocatalytic Oxidation of 2, 4-Dichlorophenol. Chemospher
653　　　　30:1385–1399

654

655

656

657

658

659

660

661

662

663

664

665

Slag + (13M) HNO₃ 1 (g): 20, 10, 5 and 3 (ml)	Slag + (13M) HNO₃ + DW
Stirring at RT	Stirring at RT 6 h
Dissolved slag solution	Dissolved slag solution
Drying at 80°C – 24 h	Drying at 80°C – 24h
Heat treatment at 1000°C -100 min	HT at 1000, 800 °C -100 min
HT samples	HT samples (1-5-75 -800 / 1000) HT samples (1-5-50 -800 / 1000)
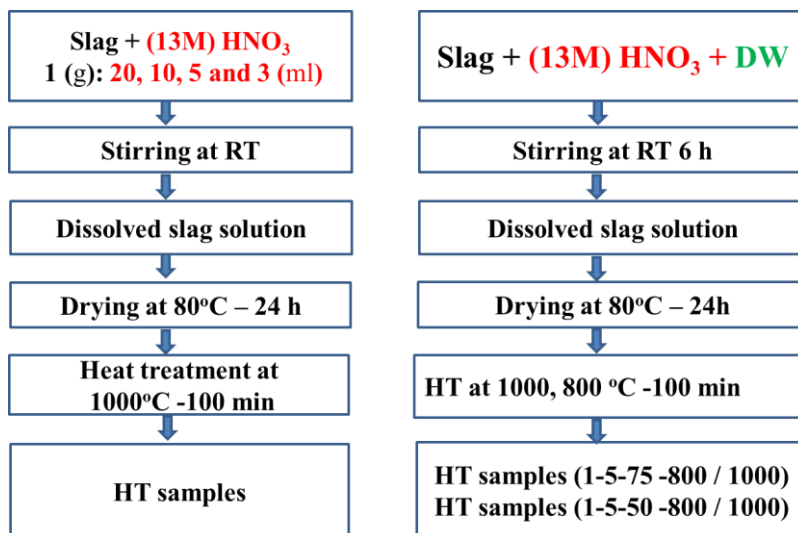
666
667
668
669
670
671
672
673
674
675
676
677
678
679
680
681
682
683
684   A. S. Ali *et al.*, Scheme 1
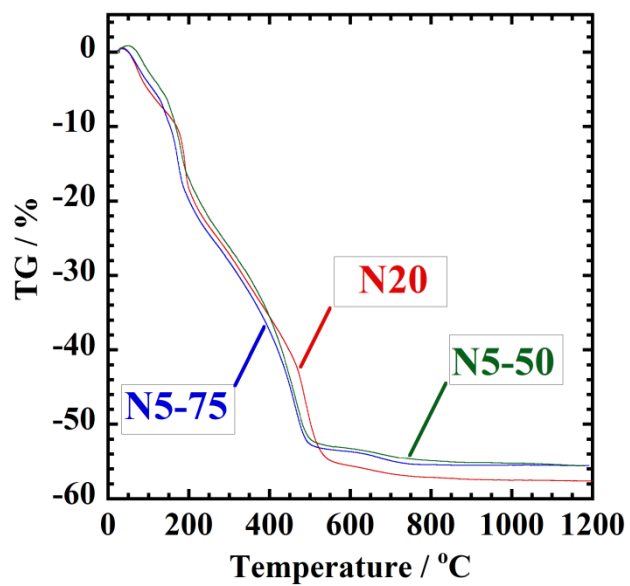
685
686
687
688
689
690
691
692
693
694
695
696
697
698
699
700
701   A. S. Ali *et al.*, Fig. 1

● **Gehlenite**   ▲ **Andradite**

■ **Essenite**   ◆**Iron silicon oxide**

★ **α-Fe₂O₃ (Hematite)**   ▼ **Calcium silicate**
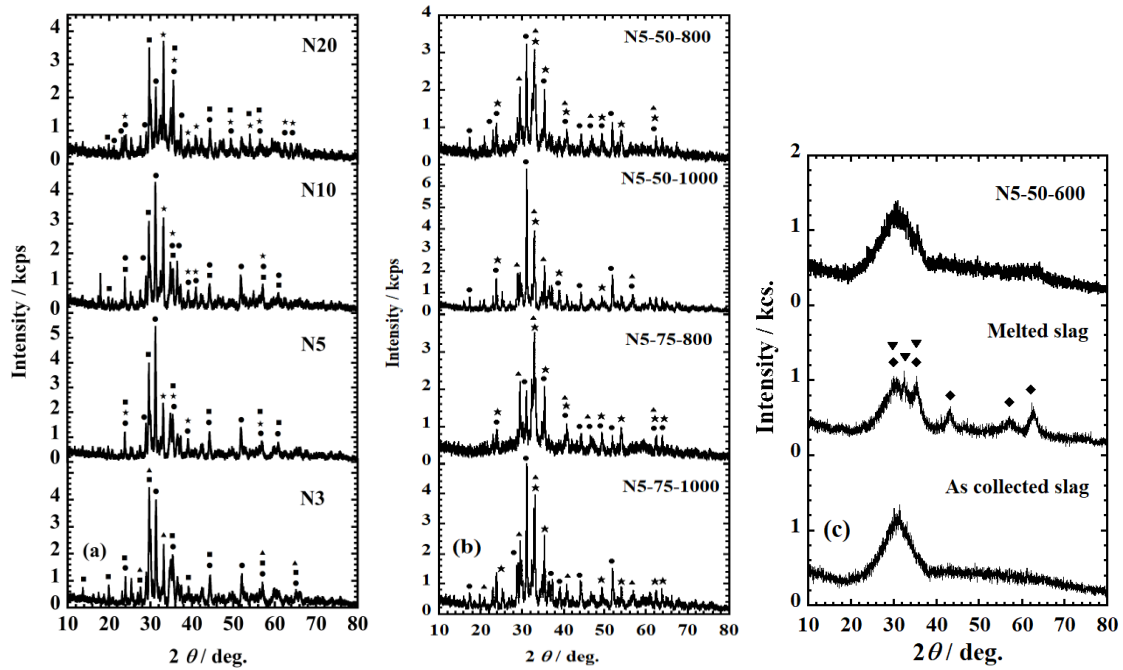
702
703
704
705
706
707
708
709
710
711
712
713
714
715
716
717   A. S. Ali *et al.*, Fig. 2 (a), (b), (c)
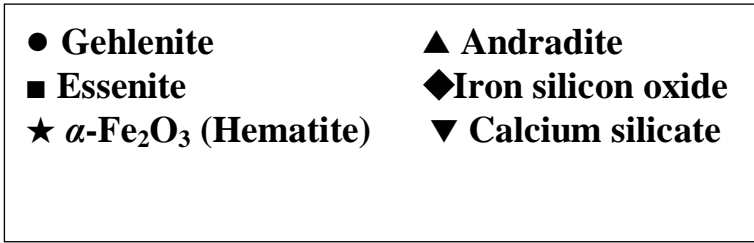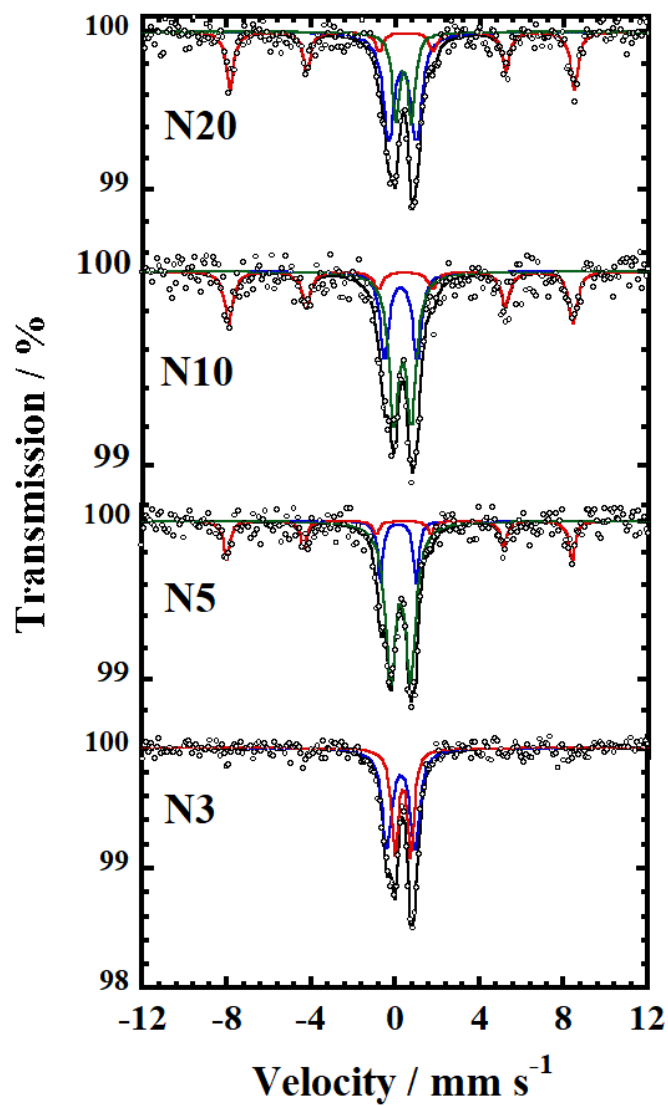
718
719
720
721
722
723
724
725
726
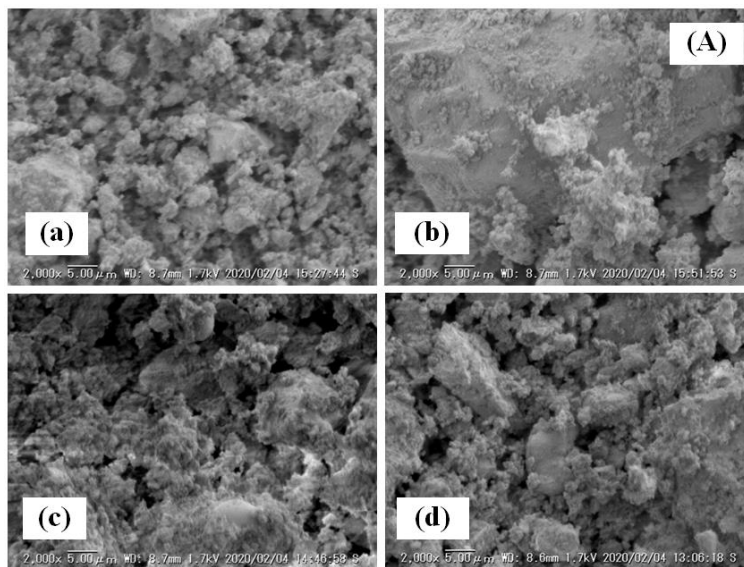727   A. S. Ali *et al.*, Fig. 3
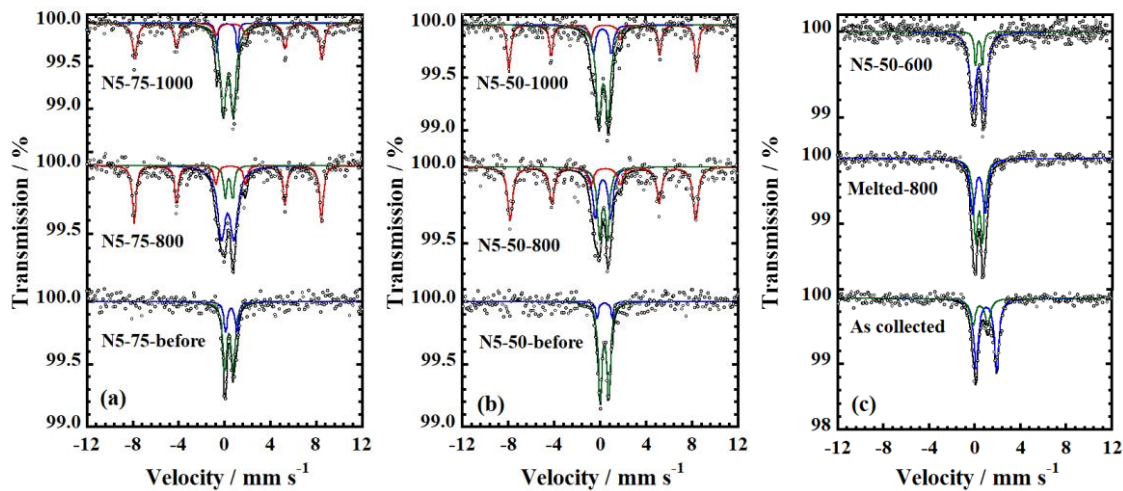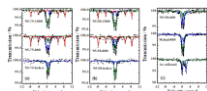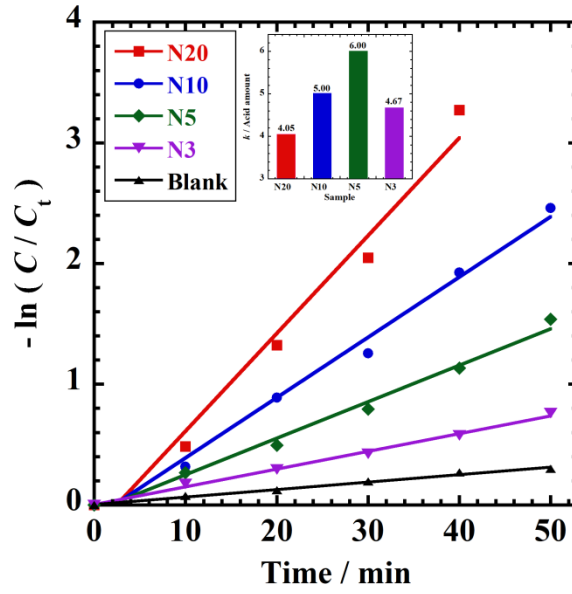
A. S. Ali *et al.*, Fig. 4 (a), (b), (c)
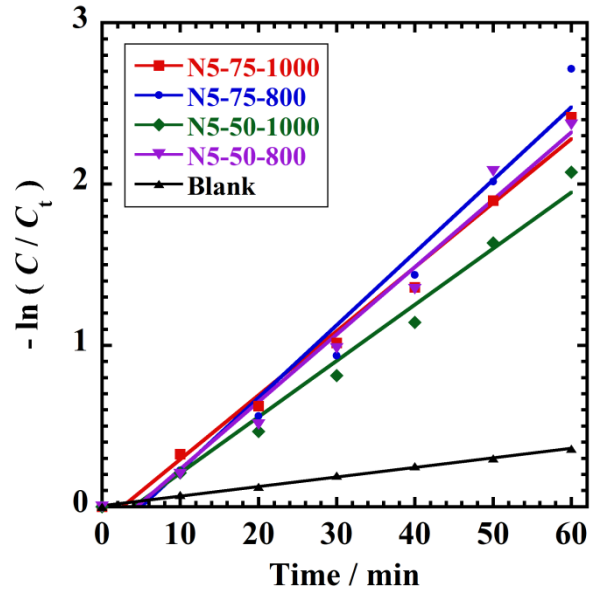
747
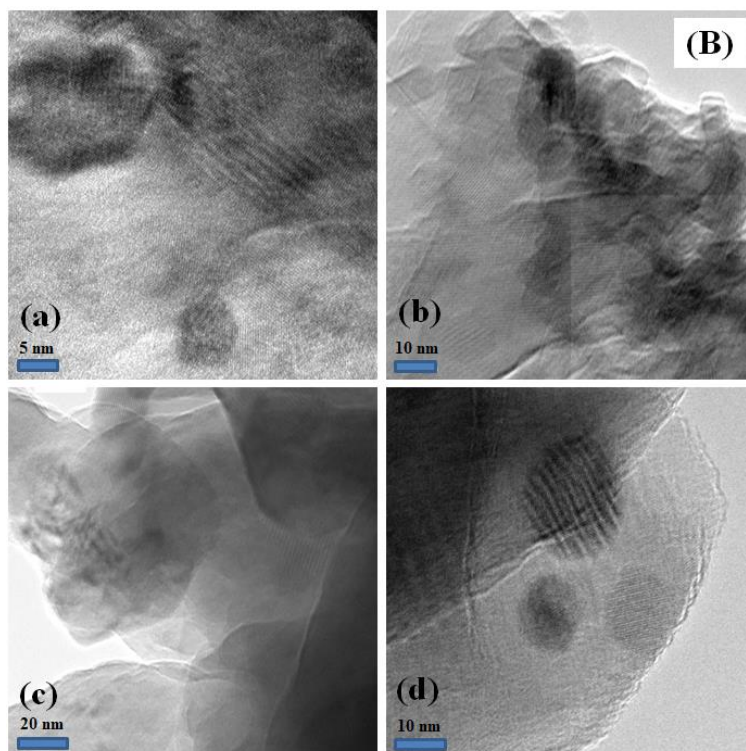
748
749

750

751

752   A. S. Ali *et al.*, Fig. 5

753
754
755
756
757
758
759
760
761
762
763
764
765
766
767
768
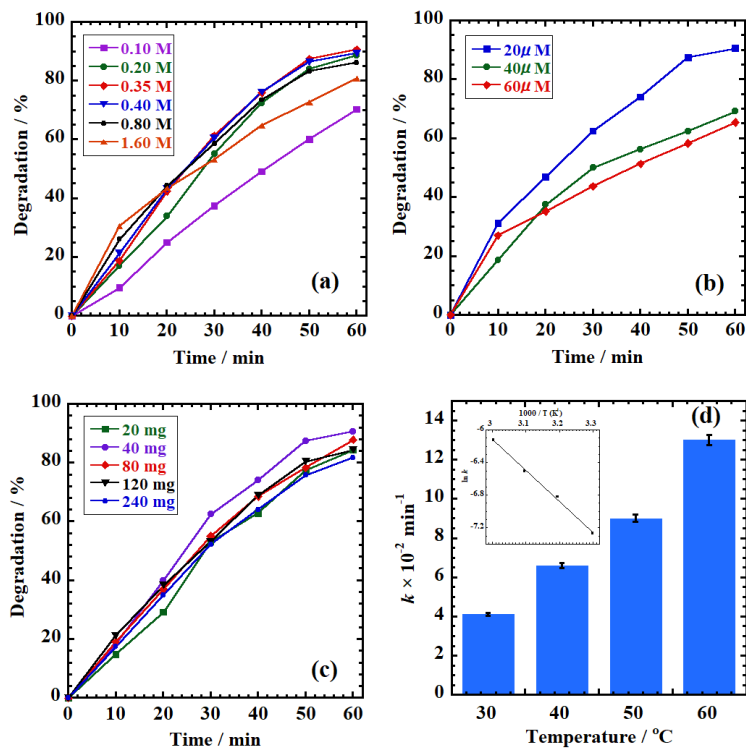769 A. S. Ali *et al.*, Fig. 6

770

771
772
773
774
775
776
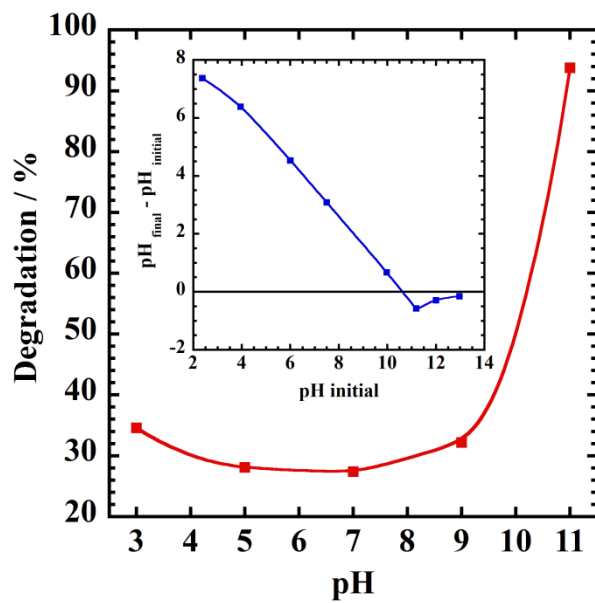777
778
779
780
781
782
783
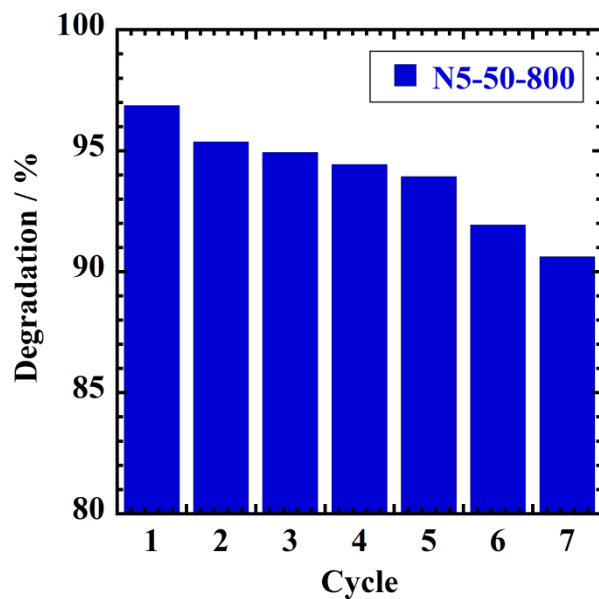784
785
786 A. S. Ali *et al.*, Fig. 7

787
788
789
790
791
792
793
794
795
796
797
798
799
800
801   A. S. Ali *et al.*, Fig. 8 (a), (b), (c), (d)

802
803
804
805
806
807
808
809
810
811
812
813
814
815
816
817
818   A. S. Ali *et al.*, Fig. 9

819
820
821
822
823
824
825
826
827
828
829
830
831
832
833
834
835   A. S. Ali *et al.*, Fig. 10

Figure Captions

Scheme 1 Schematic diagram of the sample preparation using concentrated HNO_3 (left)

and diluted HNO_3 (right)

Fig. 1 TG curves of the samples N20, N5-75 and N5-50

Fig. 2 XRD patterns of samples (a) prepared using concentrated HNO_3 heat-treated at

1000 °C for 100 min, (b) prepared using diluted HNO_3 heat-treated at 800 and 1000 °C

842   for 100 min and (c) as collected slag, melted slag heat-treated at 800 °C for 100 min and

843   the sample prepared using diluted HNO_3 heat-treated at 600 °C for 100 min

844

845   **Fig. 3** RT Mössbauer spectra of samples prepared using concentrated HNO_3 heat-treated

846   at 1000 °C for 100 min

847

848   **Fig. 4** RT Mössbauer spectra of samples prepared using diluted HNO_3 (a) 75% (b) 50%

849   and (c) as collected slag, melted slag heat-treated at 800 °C for 100 min and the sample

850   prepared using diluted HNO_3 heat-treated at 600 °C for 100 min

851

852   **Fig. 5** Images of (A) SEM and (B) TEM of the samples (a) N5-75-800 (b) N5-75-1000

853   (c) N5-50-800 (d) N5-50-1000

854

855   **Fig. 6** Kinetic dye degradation measurements of methylene blue for the samples prepared

856   using concentrated HNO_3 heat-treated at 1000 °C for 100 min under photo Fenton the

857   inset is the ratio of k and acid amount for each sample

858

859   **Fig. 7** Kinetic dye degradation measurements of methylene blue for the samples prepared

860   using diluted HNO_3 heat-treated at 800 and 1000 °C for 100 min under photo Fenton

861

862   **Fig. 8** Effect of (a) H_2O_2 concentration, (b) MB concentration, (c) catalyst (iron silicate

863   powder) loading and (d) temperature on the MB degradation for the sample N5-50 heat-

864   treated at 800 °C for 100 min

865

866   **Fig. 9** Influence of pH on the MB degradation for the sample N5-50 heat-treated at 800

867   °C for 100 min the inset is zero point of charge

868

869   **Fig. 10** Reusability of the samples N5-50-800 for MB degradation at pH 11 under

870   catalyst loading 4 g/L, MB concentration 20 μM and H_2O_2 concentration 0.35M

871

872

873 **Table 1** XRF compositional analysis of domestic waste slag (weight %) collected July
874 2018

O_3	Fe_2O_3	CaO	Na_2O	TiO_2	MgO	P_2O_5	K_2O	
30	18.33	24.61	4.69	2.14	3.12	1.45	0.21	

875
876
877
878
879
880
881
882
883
884
885
886
887
888
889
890
891
892
893
894
895
896
897
898 A. S. Ali *et al*
899 **Table 2** Composition and identification of the samples dissolved in diluted HNO_3

Slag (g)	HNO_3 (ml)	DW (ml)	HNO_3 V (%)	Sample identification (Slag-Solution-HNO_3)
1.00	3.75	1.25	75	1-5-75
1.00	2.50	2.50	50	1-5-50
1.00	1.25	3.75	25	1-5-25

900
901
902
903
904
905
906
907
908
909

910
911
912
913
914
915
916
917
918
919
920
921 A. S. Ali *et al*
922 **Table 3** Room temperature ^{57}Fe Mössbauer fitted parameters for room temperature
923 analyses of as collected slag (not heat treated), slag melted at 1400 °C; heat treated at
924 800°C for 100 min; and concentrated HNO_3 dissolved slag samples after heat treatment at
925 1000°C for 100 min

Sample	Species	A (%)	δ (mm s^{-1})	Δ (mm s^{-1})	H_{int} (T)	Γ (mm s^{-1})
N20	$Fe^{III}T_d$	44	$0.33_{\pm0.02}$	$1.30_{\pm0.10}$	-	$0.63_{\pm0.05}$
	$Fe^{III}O_h$	23	$0.39_{\pm0.02}$	$0.74_{\pm0.06}$	-	$0.40_{\pm0.09}$
	Hem	33	$0.42_{\pm0.02}$	$-0.20_{\pm0.03}$	$50.6_{\pm0.1}$	$0.42_{\pm0.05}$
N10	$Fe^{III}T_d$	25	$0.25_{\pm0.03}$	$1.55_{\pm0.16}$	-	$0.48_{\pm0.17}$
	$Fe^{III}T_d$	46	$0.34_{\pm0.03}$	$0.82_{\pm0.12}$	-	$0.56_{\pm0.10}$
	Hem	29	$0.37_{\pm0.02}$	$-0.23_{\pm0.05}$	$50.6_{\pm0.17}$	$0.48_{\pm0.08}$
N5	$Fe^{III}T_d$	13.7	$0.15_{\pm0.02}$	$1.69_{\pm0.04}$	-	$0.29_{\pm0.07}$
	$Fe^{III}T_d$	66	$0.26_{\pm0.01}$	$0.95_{\pm0.03}$	-	$0.58_{\pm0.03}$
	Hem	20.3	$0.35_{\pm0.03}$	$-0.21_{\pm0.05}$	$50.7_{\pm0.2}$	$0.35_{\pm0.08}$
N3	$Fe^{III}T_d$	57.5	$0.29_{\pm0.01}$	$1.33_{\pm0.04}$	-	$0.53_{\pm0.13}$
	$Fe^{III}O_h$	42.5	$0.38_{\pm0.01}$	$0.76_{\pm0.02}$	-	$0.37_{\pm0.03}$
Melted slag	$Fe^{III}O_h$	55.6	$0.36_{\pm0.01}$	$0.62_{\pm0.06}$	-	$0.44_{\pm0.05}$
	$Fe^{III}T_d$	44.4	$0.34_{\pm0.01}$	$1.10_{\pm0.09}$	-	$0.51_{\pm0.06}$
As collected slag	$Fe^{II}O_h$	70.2	$1.01_{\pm0.01}$	$1.81_{\pm0.02}$	-	$0.47_{\pm0.03}$
	$Fe^{III}O_h$	29.8	$0.48_{\pm0.06}$	$1.32_{\pm0.09}$	-	$0.53_{\pm0.09}$

926 *Hem.* Hematite, T_d tetrahedral, O_h octahedral, A absorption area, δ isomer shift, Δ
927 quadrupole splitting, H_{int} internal magnetic field, Γ line width
928

929
930
931
932
933
934
935 A. S. Ali *et al*

Table 4 Room temperature ^{57}Fe Mössbauer fitted parameters for room temperature analyses of diluted HNO_3 dissolved slag samples before and after heat treatment at 600, 800 and 1000°C for 100 min

Sample	Species	A (%)	δ (mm s^{-1})	Δ (mm s^{-1})	H_{int} (T)	Γ (mm s^{-1})
N5-50-1000	Fe^{III} T_d	13.6	0.24 $_{\pm 0.01}$	1.58 $_{\pm 0.06}$	-	0.46 $_{\pm 0.07}$
	Fe^{III} T_h	52.4	0.32 $_{\pm 0.01}$	0.80 $_{\pm 0.02}$	-	0.56 $_{\pm 0.04}$
	Hem	34.0	0.37 $_{\pm 0.01}$	−0.23 $_{\pm 0.03}$	50.7 $_{\pm 0.1}$	0.35 $_{\pm 0.04}$
N5-50-800	Fe^{III} T_d	23.4	0.28 $_{\pm 0.03}$	1.36 $_{\pm 0.1}$	-	0.52 $_{\pm 0.1}$
	Fe^{III} T_d	27.0	0.32 $_{\pm 0.02}$	0.69 $_{\pm 0.08}$	-	0.45 $_{\pm 0.08}$
	Hem	49.6	0.39 $_{\pm 0.02}$	−0.23 $_{\pm 0.04}$	50.1 $_{\pm 0.1}$	0.53 $_{\pm 0.07}$
N5-50-600	Fe^{III} T_d	84.0	0.32 $_{\pm 0.01}$	1.04 $_{\pm 0.06}$	-	0.58 $_{\pm 0.03}$
	Fe^{III} O_h	16.0	0.35 $_{\pm 0.02}$	0.62 $_{\pm 0.05}$	-	0.25 $_{\pm 0.08}$
N5-50-bef	Fe^{III} O_h	88.7	0.36 $_{\pm 0.01}$	0.74 $_{\pm 0.04}$	-	0.38 $_{\pm 0.04}$
	Fe^{III} O_h	10.3	0.39 $_{\pm 0.05}$	1.32 $_{\pm 0.14}$	-	0.27 $_{\pm 0.03}$
N5-75-1000	Fe^{III} T_d	7.1	0.20 $_{\pm 0.02}$	1.81 $_{\pm 0.06}$	-	0.22 $_{\pm 0.08}$
	Fe^{III} T_d	54.5	0.30 $_{\pm 0.01}$	0.88 $_{\pm 0.03}$	-	0.60 $_{\pm 0.04}$
	Hem	38.3	0.43 $_{\pm 0.02}$	−0.22 $_{\pm 0.03}$	50.6 $_{\pm 0.10}$	0.48 $_{\pm 0.06}$
N5-75-800	Fe^{III} O_h	9.9	0.36 $_{\pm 0.04}$	0.65 $_{\pm 0.06}$	-	0.33 $_{\pm 0.10}$
	Fe^{III} T_d	50.3	0.26 $_{\pm 0.02}$	1.10 $_{\pm 0.10}$	-	0.81 $_{\pm 0.06}$
	Hem	39.8	0.39 $_{\pm 0.01}$	−0.25 $_{\pm 0.02}$	50.6 $_{\pm 0.07}$	0.38 $_{\pm 0.03}$
N5-75-bef	Fe^{III} O_h	72.4	0.37 $_{\pm 0.02}$	0.73 $_{\pm 0.04}$	-	0.40 $_{\pm 0.05}$
	Fe^{III} O_h	27.6	0.57 $_{\pm 0.04}$	0.97 $_{\pm 0.08}$	-	0.34 $_{\pm 0.1}$

939 *Hem.* Hematite, T_d tetrahedral, O_h octahedral, A absorption area, δ isomer shift, Δ
940 quadrupole splitting, H_{int} internal magnetic field, Γ line width
941
942

943
944
945
946 A. S. Ali *et al*
947 **Table 5** Surface area and *k* values of the samples prepared using diluted HNO_3 and heat
948 treated at 800 and 1000 ^{o}C for 100 min

Sample	Surface area (m^2 / g)	k ($\times$ 10^{-2} min^{-1})
N5-50-800	2.63 ± 0.05	4.1 ± 0.1
N5-50-1000	2.16 ± 0.05	3.4 ± 0.1
N5-75-800	5.38 ± 0.10	4.5 ± 0.1
N5-75-1000	3.64 ± 0.07	3.9 ± 0.1

949
950
951
952
953
954
955
956
957
958
959
960
961
962
963
964
965
966
967
968
969
970 A. S. Ali *et al*
971